A Computational Method for Predicting Inferior Vena Cava Filter Performance on a Patient-Specific Basis

Kenneth I. Aycock[1,2], Robert L. Campbell[2,3], Keefe B. Manning[1,4], Shankar P. Sastry[5], Suzanne M. Shontz[6,7,8], Frank C. Lynch[4], Brent A. Craven[1,2,3]

[1]Department of Bioengineering, The Pennsylvania State University, University Park, PA; [2]Applied Research Laboratory, The Pennsylvania State University, State College, PA; [3]Department of Mechanical and Nuclear Engineering, The Pennsylvania State University, University Park, PA; [4]Department of Surgery, Penn State Hershey Medical Center, Hershey, PA; [5]Scientific Computing and Imaging Institute, University of Utah, Salt Lake City, UT; [6]Department of Mathematics and Statistics, Mississippi State University, Mississippi State, MS; [7]Department of Computer Science and Engineering, Mississippi State University, Mississippi State, MS; [8]Center for Computational Sciences, Mississippi State University, Mississippi State, MS

Abstract

A computational methodology for simulating virtual inferior vena cava (IVC) filter placement and IVC hemodynamics was developed and demonstrated in two patient-specific IVC geometries: a left-sided IVC and an IVC with a retroaortic left renal vein. An inverse analysis was performed to obtain the approximate *in vivo* stress state for each patient vein using nonlinear finite element analysis (FEA). Contact modeling was then used to simulate IVC filter placement. Contact area, contact normal force, and maximum vein displacements were higher in the retroaortic IVC than in the left-sided IVC (144 mm^2, 0.47 N, and 1.49 mm vs. 68 mm^2, 0.22 N, and 1.01 mm, respectively). Hemodynamics were simulated using computational fluid dynamics (CFD), with four cases for each patient-specific vein: 1) IVC only, 2) IVC with a placed filter, 3) IVC with a placed filter and model embolus, all at resting flow conditions, and 4) IVC with a placed filter and model embolus at exercise flow conditions. Significant hemodynamic differences were observed between the two patient IVCs, with the development of a right-sided jet, larger flow recirculation regions, and lower maximum flow velocities in the left-sided IVC. These results support further investigation of IVC filter placement and hemodynamics on a patient-specific basis.

Keywords: Computational fluid dynamics, Finite element analysis, Virtual device placement, Patient-specific modeling

Introduction

Over 900,000 patients suffer a pulmonary embolism (PE) each year in the US alone, proving fatal in as many as one-third of the cases.[49] PE occurs when an embolus obstructs pulmonary blood flow, usually as a result of deep vein thrombosis (DVT) or trauma. Clinicians traditionally treat PE with anticoagulation therapy.

When conditions such as excessive bleeding contraindicate the use of anticoagulants, an inferior vena cava (IVC) filter may instead be implanted to capture emboli upstream of the pulmonary circulation.

Though the use of IVC filters appears to be growing,[25] complications remain common.[7] A randomized trial conducted by the PREPIC (Prévention du Risque d'Embolie Pulmonaire par Interruption Cave) group[31] in 2005 found an increase in DVT in the years following IVC filter placement, possibly as a result of caval occlusion at the filter placement site. A recurrence of PE in 6.2% of patients was also noted, which suggests the escape of incoming or previously-contained emboli. It may be possible to mitigate these problems by determining which IVC filters and placement locations provide the best scenarios for embolus capture, thrombolysis, and continued caval patency. However, optimal filter selection and placement is likely to be patient-specific[42] due to anatomical variability of the IVC[51], which influences IVC hemodynamics and the embolus trapping efficiency of the placed IVC filter, and patient lung function, which influences the size of emboli that may be passed without complication.[44]

Previous experimental and computational studies have investigated the hemodynamic effects of IVC filter placement and embolus capture in simplified IVC geometries. Many *in vitro* studies have been performed using optical methods such as particle image velocimetry (PIV).[10,11,16,20,21,23,24,44,45] Studies considering placed filters have shown that IVC filter presence alone does not significantly affect blood flow;[16,23] however, the placed IVC filter does affect the location and shape of captured emboli.[44] Computational studies have also been carried out to investigate filter tilt,[41] the hemodynamic effects of captured emboli,[33,39,40,42,44,46] and to identify optimal IVC filter placement locations.[50] A patient-averaged IVC geometry based on data from ten different individuals with normal IVC anatomy was studied by Rahbar *et al.*,[33] revealing that simplified straight-tube geometries do not yield physiologically realistic flow patterns. The same patient-averaged model was later studied at rest and at exercise flow conditions.[34]

Besides the preliminary study by Sastry *et al.*,[39] a true "patient-specific" study that considers variable IVC morphology and *in vivo* placement of an IVC filter, and the resultant IVC hemodynamics, is lacking. The objective of this study is to demonstrate a computational methodology for assessing the effects of IVC filter placement and embolus capture on a patient-specific basis. Two anatomical variants not previously considered in experimental or computational flow studies are investigated to demonstrate the methodology and to provide insight into the clinical relevance of these IVC anomalies.

Methods

Computational Models

Computational models of the patient IVCs, an IVC filter, and an idealized embolus were created to simulate the effects of IVC filter placement and embolus capture. Patient-specific IVC models were reconstructed from

patient computed tomography (CT) data. Specifically, after obtaining Institutional Review Board exemption (Penn State Hershey Medical Center), veins were imaged with 0.87 mm per pixel in-plane resolution and 1.5 mm per pixel out-of-plane resolution.[39] Two IVC anomalies were chosen: a left-sided IVC (0.2-0.5% of the population) and an IVC with a retroaortic left renal vein (1.7-3.4% of the population).[51] The CT data was segmented in Amira (Visualization Sciences Group, Burlington, MA), then assembled using the marching cubes algorithm to obtain surface meshes of each patient vein (Fig. 1a and 1b). The surface meshes were smoothed using the volume-conserving Humphrey's Classes Laplacian algorithm available in Meshlab (Visual Computing Lab, ISTI, CNR).

The G2 Express IVC filter (Bard Peripheral Vascular, Tempe, AZ) was selected for this study because of previous experience with this device at the Penn State Hershey Medical Center. A computer aided design (CAD) model of the filter was created in NX 6.0 (Siemens PLM Software Co., Plano, TX). All features of the filter were modeled, including the filter hub, struts, and strut hooks (Fig. 1c).

A model embolus was created to simulate IVC hemodynamics following embolus capture in the IVC filter. Captured emboli reduce the available flow area of the IVC, increasing the velocity of the flow locally and potentially affecting the flow downstream. The altered flow may be thrombogenic, or may promote embolus dissolution. In order to investigate these conditions, a teardrop-shaped geometry similar to the emboli used by other authors[11,16,23,24,33,44] was created with a volume of 0.63 cm^3 (Fig. 1d), which lies in the range of emboli observed clinically in IVC filters.[47]

[Figure 1 about here.]

Patient-Specific Filter Placement

Virtual IVC filter placement was performed using the commercial finite element analysis (FEA) program ABAQUS version 6.12 (Simulia, Dassault Systèmes, Providence, RI). Following the pre-processing tasks of mesh generation and material property assignment, virtual IVC filter placement was accomplished in two simulation stages: an inverse analysis stage to obtain the approximate *in vivo* stress state of each patient vein and a contact modeling stage to simulate the interactions between the IVC filter and the vein wall during filter placement.

Finite element meshes were generated for the patient IVCs and the IVC filter. To reduce computational cost, the infrarenal portion of each patient IVC was isolated to create smaller surface meshes, which had average hydraulic diameters of approximately 18 mm (left-sided IVC) and 14 mm (retroaortic IVC). These surface meshes were then extruded at a uniform thickness of 0.831 mm, representative of an average healthy IVC,[19] to obtain solid meshes with about 25,000 (retroaortic IVC) to 40,000 (left-sided IVC) nodes (Fig. 2a). Hybrid triangular prism elements with quadratic displacement and linear pressure interpolation (i.e., C3D15H) were used to accurately model the veins. The IVC filter was meshed using the CAD model and an

ABAQUS/CAE tool for structured meshing, yielding a mesh with about 75,000 nodes (Fig. 2b). C3D20R elements were chosen for their accuracy in problems with large distortions and bending loads.

[Figure 2 about here.]

Nonlinear material models were used for the patient veins and the IVC filter. The vein tissue was modeled as an anisotropic, hyperelastic material using the Holzapfel-Gasser-Ogden (HGO) formulation.[13,17] Local material directions were assigned to the veins using cylindrical coordinate systems (Fig. 3a). Because the actual patient-specific material properties are unknown, approximate average values were obtained from a study on the tensile properties of human IVCs[43] and fit to the HGO model to obtain the stress-stretch curves seen in Fig. 3b. The superelastic response of the nitinol IVC filter was modeled using a built-in ABAQUS user-material subroutine based on the constitutive equation proposed by Auricchio and Stefanelli[3] for superelastic alloys. Material properties for nitinol were obtained from Conti.[9]

[Figure 3 about here.]

Inverse Analysis

An inverse analysis was performed on each patient vein to obtain approximate *in vivo* stress states. In general, an inverse analysis is a process used to obtain a reference configuration when the deformed configuration and boundary conditions are known. In this study, the objective of the inverse analysis was to determine the approximate zero-load configuration of each patient vein knowing the *in vivo* configuration (from CT data) and approximate *in vivo* boundary conditions. This is necessary since the material properties were obtained from *ex vivo* vein specimens starting in the zero-load state. Once the zero-load geometries are found, it is possible to re-obtain the *in vivo* geometries along with the approximate *in vivo* stresses by applying representative boundary conditions. The method presented here is similar to that used by others to estimate *in vivo* stresses in patient-specific arteries.[12,18]

The inverse analysis was an iterative process consisting of three repeated steps: 1) application of estimated *in vivo* boundary conditions, 2) error calculation, and 3) generation of a new geometry approaching the unloaded state of the IVC (Fig. 4). Boundary conditions on the patient veins consisted of a 15% axial stretch,[43] and a net internal pressure of 2 mmHg. Here 'net' refers to a balance of the internal and external pressures on the vessel, which were assumed to be close to the central venous pressure ($\sim$9 mmHg[28]) and the intra-abdominal pressure ($\sim$7 mmHg[38]), respectively. Though the actual net pressure on the IVC wall changes from patient-to-patient with respiration, activity, and the location of surrounding organs, a constant pressure in the physiological range was used here for simplicity. Longitudinal motion of the vein ends was specified with displacement constraints, while the vein ends were allowed to expand or contract radially as in Auricchio *et al.*[2]

A MATLAB (Mathworks, Natick, MA) script was used to execute the inverse analysis. To begin, each starting vein geometry, originating from the patient CT data, was loaded into an array. ABAQUS/Implicit was then called to apply the boundary conditions to the vein geometry stored in memory. Error at each node was calculated by comparing the results to the starting geometry. The analysis was considered converged once the average nodal error was less than approximately 1e-4 mm. If the nodal error exceeded this tolerance, a new geometry was created by subtracting a percentage of the error at each node from the input geometry and beginning a new iteration. The process was repeated until the specified tolerance was satisfied.

Refinement of the retroaortic IVC mesh from 25,000 nodes to 72,000 nodes resulted in less than 0.1% change in average nodal displacement, demonstrating that the coarser mesh resolution was sufficient. Simulations were performed on 16 processors and required about 12 hours of wall time to complete.

[Figure 4 about here.]

Contact Modeling

After obtaining the estimated *in vivo* stress state for each patient vein, IVC filter placement was simulated using contact modeling. Contact surfaces were defined for the IVC filter, the patient IVC, and a 10F (3.33mm) catheter. The node-to-surface, finite-sliding contact formulation in ABAQUS was used. The IVC filter was first drawn into the catheter, which was modeled as a rigid tube. The insertion end of the tube was flared out to reduce numerical discontinuities during the transition of the IVC filter from the open to the compressed state. Once the IVC filter was fully inserted into the catheter, it was positioned inside the patient IVC, with the IVC in the *in vivo* stress state obtained from the inverse analysis.

The filter was then virtually placed in the patient vein by removing the contact constraints between the IVC filter and the catheter, while applying contact constraints between the IVC filter and the patient vein. The IVC filter strut hooks were not included in the IVC filter contact surface (Fig. 2b-*) under the assumption that the strut hooks embed into the vein wall, which agrees with previous studies[11,44,46] and clinical observations. A high friction coefficient (2.0) was used at the interface between the strut ends and the IVC vein wall to simulate the resistance to movement provided by the strut hooks and to obtain a stable placed state. A low friction coefficient (0.02) was used on the rest of the IVC filter surface, similar to that used in other virtual device placement studies.[27]

The implicit solver for ABAQUS was also used for the contact modeling simulations. Automatic stabilization was enabled to dampen oscillations and improve convergence. Some simulations converged without the use of automatic stabilization; a comparison of simulation results with and without stabilization in these cases showed that the stabilization parameter did not introduce significant error into the results. Refinement of the IVC filter mesh from 75,000 nodes to 111,000 nodes resulted in no significant difference in IVC filter displacements, demonstrating that the coarser filter mesh resolution was sufficient. Simulations were

performed on 16 processors and required 12 to 24 hours of wall time to complete.

Patient-Specific Hemodynamics

Computational fluid dynamics (CFD) simulations of blood flow were carried out using the deformed vein and filter geometries and the open-source CFD software OpenFOAM (OpenCFD, Ltd). This involved generating computational meshes, specifying physiologically-realistic flow properties and boundary conditions, and running the CFD calculations on a high-performance parallel computer cluster. Computational meshes of each patient vein, pre- and post- IVC filter placement, were created using the hexahedral-dominant, unstructured mesh generation utility, snappyHexMesh, available in OpenFOAM. Multiple meshes, ranging from approximately 3 to 11 million computational cells, were generated to carry out a CFD mesh refinement study. All meshes included several wall-normal layers on the vein walls to accurately resolve large, near-wall velocity gradients (Figure 5).

[Figure 5 about here.]

Blood was modeled as an incompressible, Newtonian fluid with a constant density, $\rho = 1{,}060$ kg m^{-3}, and kinematic viscosity, $\mu = 4.4$ cSt (representative of blood undergoing a shear rate of about 50 s^{-1}).[36] Though blood is a non-Newtonian fluid, Swaminathan *et al.*[46] showed that the Newtonian approximation introduces $< 10\%$ error when simulating flow in the IVC. Given a maximum Reynolds number based on vein diameter of approximately 1400, laminar flow was assumed for all cases. Moreover, previous studies have found that transitional flow does not have a significant impact on the overall flow through the IVC.[34]

[Table 1 about here.]

Boundary conditions were specified for each case to simulate physiological conditions. Fully-developed flow was assumed at each of the inlets. Because the cross-sections of the inlets were not circular, inlet flow profiles were first computed by extruding the inlets beyond their entry lengths and obtaining steady-state flow solutions. The resulting flow profiles were mapped onto the inlets of the patient veins. Flow rates were specified based on empirical data from Cheng *et al.*,[6] with total resting and exercise flow rates of 2.0 lpm and 5.5 lpm, respectively (Table). A constant-pressure outflow boundary condition was specified at the outlet in each patient vein. A no-slip boundary condition was specified on the surfaces of the vein walls, the IVC filter, and the embolus.

Simulations of blood flow under resting conditions allowed for the use of a steady-state flow solver. The Semi-Implicit Method for Pressure-Linked Equations (SIMPLE) algorithm available in OpenFOAM was used to solve the incompressible continuity and Navier–Stokes equations governing steady, laminar flow with second-order accurate spatial discretization schemes. Iterative convergence of the SIMPLE solver was guaranteed by ensuring that the solution residuals were reduced to less than 10^{-3}. Additionally, the solution

variables (e.g., inlet pressures, viscous and pressure forces on the embolus, and the outlet flow rates) were monitored to ensure convergence of the computed flow field. All simulations were run on 80 processors, with wall times ranging from 4 to 12 hours.

For cases that included a placed embolus under exercise flow conditions, convergence of the steady-state flow solver stalled due to the development of unsteady flow downstream of the embolus. Thus, a transient flow solver based on the PIMPLE (hybrid PISO/SIMPLE[30]) algorithm was used to obtain time-accurate solutions, using second-order accurate temporal discretization and a variable time step size that was automatically adjusted to maintain a Courant number of approximately 40. Transient simulations were performed until the solution reached a statistically-stationary state, after which the flow solution was sampled and time-averaged over one second of physical time, corresponding to approximately one IVC flow-through time (defined as the IVC volume divided by the volumetric flow rate through the IVC). Simulations were run on 80 processors, with wall times ranging from 24 to 72 hours.

Finally, a mesh refinement study was performed to estimate the numerical error present in the CFD solutions. This was done using the retroaortic case with the placed filter and captured embolus at the highest flow rate (exercise flow conditions), since this was the most limiting case in terms of mesh resolution requirements. Three mesh resolutions were evaluated: coarse (2.7 million cells), medium (5.4 million cells), and fine (10.7 million cells). Mesh refinement resulted in $< 0.1\%$ change in overall pressure drop across the model, while the viscous and pressure forces on the embolus changed more significantly; for this reason, the total force on the placed embolus was selected as the parameter for estimating grid convergence error. Using Richardson extrapolation theory,[35] the grid convergence index (GCI) was calculated to be 2.68% (using a factor of safety of 1.25 as recommended by Roache[35]) for the fine mesh, indicating that this level of mesh resolution accurately captures the flow physics and that the fine mesh CFD solution is "mesh-independent."

Cases

Four cases were considered for each patient-specific vein: 1) IVC only, 2) IVC with a placed filter, 3) IVC with a placed filter and a model embolus, all at resting flow conditions, and 4) IVC with a placed filter and a model embolus at exercise flow conditions. These cases cover the range of physiological conditions likely to occur *in vivo*.

Results

Patient-Specific Filter Placement

The inverse analyses reached convergence in 100 to 150 iterations for each patient vein. A maximum nodal error of 0.015 mm was obtained, which is significantly less than the resolution of the original CT data.

Approximate *in vivo* stress states were calculated, yielding regions of high and low stress (Fig. 6c). The resultant zero-load states were shorter axially and wider circumferentially than the starting geometries. Some buckling was also observed in the zero-load states (see Fig. 6b).

[Figure 6 about here.]

Contact modeling simulations (Fig. 7) resulted in maximum vein displacements of approximately 5% (1.01 mm) and 10% (1.49 mm) of the IVC diameters in the left-sided and retroaortic IVCs, respectively. The largest vein displacements occurred at the interface between the vein wall and the first bend in the IVC filter struts without hooks (Fig. 9a-i and 9b-i). Virtual IVC filter placement yielded a higher contact area and total outward normal contact force in the retroaortic IVC than in the left-sided IVC (144 mm^2 and 0.47 N vs. 68 mm^2 and 0.22 N, respectively). In the retroaortic case, a hook on one of the left-sided filter struts did not embed, as expansion of the strut was inhibited by the vein wall (Fig. 7c-*). Overall, the retroaortic IVC was more deformed (0.33 ml or 7.7% increase in infrarenal volume) by IVC filter placement than was the left-sided IVC (0.21 ml or 2.1% increase in infrarenal volume).

The opening angle of the inner IVC filter struts was similar in each patient vein at about 25°. This allowed for the use of the same model embolus in each patient-specific case. Embolus placement resulted in a maximum of 38% occlusion of the IVC cross-sectional area in the retroaortic IVC, while a maximum of 22% of the left-sided IVC was occluded by the embolus.

[Figure 7 about here.]

Patient-Specific Hemodynamics

CFD results were obtained for each patient IVC at resting and exercise conditions. Velocity and wall shear stress (WSS) fields varied significantly between the two patient-specific models as described in the following.

Velocity

Differences in IVC flow patterns between the two patient-specific models were apparent prior to filter and embolus placement. In the left-sided IVC, a right-sided jet developed in the infrarenal region, beginning at the confluence of the iliac veins and ending at the entrance of the renal veins (Fig. 8-i). A naturally occurring recirculation zone also developed adjacent to this jet on the left side of the left-sided IVC (Fig. 8-ii). In the retroaortic IVC, flow was more uniformly distributed, especially in the infrarenal region (Fig. 8-viii). Average and maximum velocities were higher in the retroaortic IVC than in the left-sided IVC (Fig. 8).

Introduction of an IVC filter into the patient vein models resulted in some minor alteration of the flow. In the left-sided IVC, a small stagnation region appeared near the filter hub (Fig. 8-iii) and the recirculation

zone that existed prior to IVC filter placement decreased in size (Fig. 8-iv). In the retroaortic IVC, flow diverged around the filter hub, then converged downstream in the suprarenal IVC (Fig. 8-ix). In both patient IVCs, the presence of the filter struts near the vein walls resulted in lower near-wall flow velocities (Fig. 9).

Placement of the embolus further influenced the IVC flow patterns. In the left-sided IVC, a small recirculation region formed on the right side of the embolus, downstream from the maximum embolus diameter (Fig. 8-v and 9a-ii,iii). Also, recirculation in the left side of the IVC was further reduced due to the presence of the embolus (Fig. 8a-vi). In the retroaortic IVC, flow around the embolus was mostly uniform, with a ring of recirculating flow around the embolus downstream from the maximum embolus diameter (Fig. 9b-ii).

Exercise flow conditions resulted in larger maximum and minimum axial velocities in both patient IVCs. In the left-sided IVC, a large recirculation zone developed in the left side, larger than the recirculation region that existed in the same location prior to filter and embolus placement (Fig. 8-vii). The region of recirculating flow on the downstream end of the embolus also shifted further right, while a smaller recirculation region developed on the left side of the embolus (Fig. 9a-iv). In the retroaortic IVC, the recirculation region on the downstream end of the embolus grew, particularly on the left side (Fig. 9b-iii).

[Figure 8 about here.]

[Figure 9 about here.]

WSS

Prior to filter and embolus placement, WSS in the infrarenal region of each patient IVC was quite similar and ranged from 0 to 20 dynes cm^{-2} (Fig. 10). WSS was higher on the right side of both IVCs than on the left side. Values of WSS greater than 20 dynes cm^{-2} occurred in the left-sided IVC where the left iliac vein joins the infrarenal region and in the retroaortic IVC where the left renal vein intersects the main IVC.

Filter and embolus placement altered the WSS contours on the vein walls in some cases. Following filter placement, WSS on the vein walls near and downstream of the IVC filter struts decreased in both patient veins; this decrease in WSS was more pronounced in the retroaortic IVC, where more IVC-IVC filter contact occurred (Fig. 10-i,ii). At resting flow conditions with the placed filter and model embolus, the WSS on the left-sided IVC was mostly unaffected. Embolus presence in the retroaortic vein, however, caused the WSS to double near the region of maximum embolus diameter and IVC occlusion (Fig. 10-iii). The exercise flow rate yielded similar patterns in WSS on both patient IVCs, while the WSS magnitude increased by a factor of approximately five.

WSS was also quantified on the surfaces of the placed IVC filter and model embolus. In both patient IVCs, large WSS values were concentrated on the upstream side of the embolus (Fig. 11). In the left-sided

IVC, WSS was greatest on the right side of the embolus in the region encountered by the right-sided jet (Fig. 11-i,ii). In the retroaortic IVC, WSS on the embolus was more uniformly distributed on the upstream side. Further, in the retroaortic case the maximum WSS on the placed embolus was about twice as high as the WSS on the vein in both resting and the exercise conditions.

[Figure 10 about here.]

[Figure 11 about here.]

Discussion

A computational methodology for simulating IVC filter placement and the resulting hemodynamics was developed and demonstrated on two patient-specific IVC geometries. Virtual IVC filter placement yielded over twice as much contact area and normal contact force in the left-sided IVC than in the retroaortic IVC. The IVC hemodynamics were also shown to differ significantly between the two patient models with more asymmetric flow patterns and larger recirculation regions in the left-sided IVC than in the retroaortic IVC.

Unlike previous computational studies, which considered blood flow in idealized IVC geometries without IVC-IVC filter interations,[33,40,42,44,46] the present study addresses new aspects of IVC filter placement: 1) the *in vivo* stress state of the IVC, 2) the IVC and IVC filter deformations following IVC filter placement, and 3) the hemodynamics in IVC anomalies pre- and post- IVC filter placement. Furthermore, the preliminary work[39] and this study constitute the first attempt at virtual IVC filter placement in patient-specific IVC geometries.

Patient-Specific Filter Placement

An inverse analysis method was used to obtain the approximate *in vivo* stress state of the patient veins, in a manner similar to de Putter *et al.*,[12] who used a comparable "backward incremental method" for calculating the approximate *in vivo* stress state of abdominal aortic aneurysms. As a result, the *in vivo* stresses yielded veins that were less compliant than if the starting patient geometries had been used without *in vivo* stress. That is, had the patient-specific IVCs and the HGO model been used assuming a zero-stress state, the filter-induced vein deformations would have been overestimated and the IVC diameters following filter placement would have been greater than were obtained by starting with the approximate *in vivo* stress state of the vein. Additionally, though the filter-induced deformations were only 10% of the vein diameter, the geometry of the placed filter yielded the filter opening angle, which was needed for placement of a realistic captured embolus.

The present virtual IVC filter placement methodology also yielded contact forces and contact areas at the IVC-IVC filter interface that could be used in filter migration studies, and stresses in the vein walls

that may be useful for predicting vein wall damage or filter penetration. Such information would not be available without modeling device placement. While some similar virtual device placement studies have been performed previously,[2,27] this work constitutes the first of such attempt with an IVC filter.

Patient-Specific Hemodynamics

Slow or stagnant flow has been shown to have a thrombogenic effect due to fibrin accumulation and the development of local hypoxia.[4,26] Interestingly, a large recirculating flow region occurred in the left-sided IVC prior to IVC filter placement. Though other studies have noted naturally-occurring stagnant flow regions downstream of the renal inflow,[34,50] this is the first report of flow recirculation in the infrarenal IVC. This may be clinically significant, as higher occurrence rates of DVT have been reported in patients with IVC anomalies.[1,5,8,29,32] Near-stagnant, recirculating flow also occurred downstream of the IVC filter following embolus placement in each patient IVC, with larger recirculation regions in the left-sided IVC. Thrombolysis would be suppressed in these regions, while embolus growth may occur.

In vitro studies have shown that regions of low WSS (<1 dynes cm^{-2})[14] and high WSS (50 to 100 dynes cm^{-2})[48] can also be thrombogenic due to the influence of these stresses on certain cellular signaling processes. Low WSS occurred near the filter-vein and filter-embolus interfaces in both patient IVCs, which could lead to thrombogenesis and caval occlusion over time. The region of low WSS near the IVC-IVC filter interface was larger in the retroaortic IVC due to a greater IVC-IVC filter contact area, which indicates a greater risk of intimal hyperplasia at this location in this patient case. In the left-sided IVC, a large region of low WSS occurred on the left-side of the infrarenal vein wall near the flow recirculation region, further increasing the risk for thrombus formation in this area and also potentially leading to intimal hyperplasia.

High values of WSS occurred during resting conditions on the filter struts in regions subject to cross flow and on the upstream surface of the model embolus in both patient IVCs, and on the retroaortic IVC wall near the placed embolus. Under exercise flow conditions, high WSS occurred again on the upstream surface of the placed embolus, as well as on the retroaortic IVC wall near the placed embolus. While these areas of high WSS could cause platelet activation, high WSS can also lead to thrombolysis.[15,22,37] Thus, the exact effect of the flow on the embolus is difficult to determine, though we speculate that the embolus would remodel over time to minimize the hemodynamic forces.

Study Limitations

Virtual filter placement was limited by the lack of patient-specific data that was available beyond the *in vivo* three-dimensional reconstruction of the IVC from patient CThe T data. Though average vein material properties were used, vein properties are known to widely vary from patient-to-patient; for example, the veins of younger patients are generally more distensible than the veins of older patients. Structural

boundary conditions on the IVC could also be highly patient-specific, which would affect the results of the inverse analysis procedure and the resultant *in vivo* stress state. Future studies would benefit from more comprehensive IVC material property data, such as population statistics and trends with age, sex, smoking, etc., or patient-specific material property estimation via a non-invasive method (e.g. ultrasound).

Flow simulations were also limited by a lack of patient-specific data and assumptions made about the flow. First, fluid properties and flow boundary conditions were based on averages from the literature, while these parameters are likely to be patient-specific. Second, blood was modeled as a Newtonian fluid, despite its non-Newtonian nature. While previous idealized studies have shown that the Newtonian assumption introduces little error,[46] patient-specific studies may be more sensitive. Third, IVC compliance was modeled only during filter placement; the IVC, IVC filter, and model embolus were all assumed to be rigid in the flow simulations. In reality, the geometry of the IVC varies with respiration and flow rate.[6] Blood pulsatility was also neglected, which could have some influence on the geometry of the IVC, though the pulsatility is much lower in the IVC than in the arterial circulation. Compliance of the entire IVC / IVC filter / embolus system could be accounted for by using fluid-structure interaction (FSI) simulations in future work.

Only one IVC filter, the Bard G2 Express, was considered. Newer models from Bard have now received 510(k) clearance, including Eclipse (an electropolished version of G2 Express), Meridian, and Denali. The G2 Express was chosen, however, since it is still used clinically at many hospitals, including the Penn State Hershey Medical Center.

Summary

1. A novel computational method for simulating the effects of IVC filter placement and embolus presence on blood flow in patient-specific geometries was developed and demonstrated.

2. An inverse analysis procedure was implemented, producing approximate *in vivo* stress states for the patient veins. This method allowed for the use of *ex vivo* material property data.

3. Virtual IVC filter placement was achieved with contact modeling, which yielded maximum vein displacements of about 5-10% of the IVC diameter.

4. In the two patient IVCs studied, IVC-IVC filter contact area increased with decreasing IVC diameter.

5. One IVC filter strut hook did not embed in the retroaortic IVC. Other patient vein geometries may likewise result in placed IVC filter configurations where the IVC filter is not anchored by every strut hook, increasing the possibility for filter migration.

6. Different patient geometries resulted in significantly different flow fields, some of which may be thrombogenic. Embolus placement resulted in small regions of flow recirculation, which could result in

thrombus growth. Flow through the left-sided IVC resulted in a large recirculation region prior to filter or embolus placement, which may have contributed to the patient's disease. Other patient IVCs and IVC anomalies may produce similar flow disturbances; thus, further studies on patient-specific IVC filter placement and hemodynamics are of interest.

Acknowledgements

The authors would like to thank Jibum Kim for his assistance in segmenting and reconstructing the patient CT data. The authors also thank Rick Schraf and Todd Fetterolf for creating the CAD model of the IVC filter. This research was supported by the Walker Assistantship program at the Penn State Applied Research Laboratory.

References

[1] W. C. Ang, T. Doyle, and M. D. Stringer. Left-sided and duplicate inferior vena cava: A case series and review. *Clin. Anat.*, 2012.

[2] F. Auricchio, M. Conti, M. De Beule, G. De Santis, and B. Verhegghe. Carotid artery stenting simulation: from patient-specific images to finite element analysis. *Med. Eng. Phy.*, 33:281–9, 2011.

[3] F. Auricchio and U. Stefanelli. Numerical analysis of a three-dimensional super-elastic constitutive model. *Int. J. Numer. Meth. Eng.*, 61:142–155, 2004.

[4] E. G. Bovill and A. van der Vliet. Venous valvular stasis-associated hypoxia and thrombosis: what is the link? *Annu. Rev. Physiol.*, 73:527–45, 2011.

[5] Y. L. Chee, D. J. Culligan, and H. G. Watson. Inferior vena cava malformation as a risk factor for deep venous thrombosis in the young. *Brit. J. Haematol.*, 114:878–80, 2001.

[6] C. P. Cheng, R. J. Herfkens, and C. A. Taylor. Inferior vena caval hemodynamics quantified in vivo at rest and during cycling exercise using magnetic resonance imaging. *Am. J. Physiol. Heart Circ. Physiol.*, 284:H1161–7, 2003.

[7] J. Cipolla, N. S. Weger, R. Sharma, S. P. Schrag, B. Sarani, M. Truitt, M. Lorenzo, C. A. Sims, P. K. Kim, D. Torigian, B. Temple-Lykens, C. P. Sicoutris, and S. P. Stawicki. Complications of vena cava filters : A comprehensive clinical review. *OPUS 12 Scientist*, 2:11–24, 2008.

[8] S. Cizginer, S. Tatli, J. Girshman, J. A. Beckman, and S. G. Silverman. Thrombosed interrupted inferior vena cava and retroaortic left renal vein mimicking retroperitoneal neoplasm. *Abdom. Imaging*, 32:403–6, 2007.

[9] M. Conti. Finite element analysis of self-expanding braided wirestent. Master's thesis, Ghent University, Belgium, 2007.

[10] G. G. Couch, K. W. Johnston, and M. Ojha. An in vitro comparison of the hemodynamics of two inferior vena cava filters. *J. Vasc. Surg.*, 31:539–549, 2000.

[11] G. G. Couch, H. Kim, and M. Ojha. In vitro assessment of the hemodynamic effects of a partial occlusion in a vena cava filter. *J. Vasc. Surg.*, 25:663–72, 1997.

[12] S. de Putter, B. J. B. M. Wolters, M. C. M. Rutten, M. Breeuwer, F. A. Gerritsen, and F. N. van de Vosse. Patient-specific initial wall stress in abdominal aortic aneurysms with a backward incremental method. *J. Biomech.*, 40:1081–90, 2007.

[13] T. C. Gasser, R. W. Ogden, and G. A. Holzapfel. Hyperelastic modelling of arterial layers with distributed collagen fibre orientations. *J. R. Soc. Interface*, 3:15–35, 2006.

[14] M. S. Goel and S. L. Diamond. Adhesion of normal erythrocytes at depressed venous shear rates to activated neutrophils, activated platelets, and fibrin polymerized from plasma. *Blood*, 100:3797–803, 2002.

[15] E. F. Grabowski. Thrombolysis, flow, and vessel wall interactions. *J. Vasc. Interv. Radiol.*, 6:25S–29S, 1995.

[16] A. Harlal, M. Ojha, and K. W. Johnston. Vena cava filter performance based on hemodynamics and reported thrombosis and pulmonary embolism patterns. *J. Vasc. Interv. Radiol.*, 18:103–15, 2007.

[17] G. A. Holzapfel, T. C. Gasser, and R. W. Ogden. A new constitutive framework for arterial wall mechanics and a comparative study of material models. *J. Elasticity*, 61:1–48, 2000.

[18] X. Huang, C. Yang, C. Yuan, F. Liu, G. Canton, J. Zheng, P. K. Woodard, G. A. Sicard, and D. Tang. Patient-specific artery shrinkage and 3D zero-stress state in multi-component 3D FSI models for carotid atherosclerotic plaques based on in vivo MRI data. *Mol. Cell. Biomech.*, 6:121–134, 2009.

[19] M. Ito, C-T. Hsu, S. Shikuwa, Y. Kawase, K. Matsumoto, I. Sekine, and H. Fujii. Morphometrical study on the sclerotic inferior vena cava in chronic lung disease. *Acta Med. Nagasaki*, 33:157–162, 1988.

[20] H. J. Jaeger, S. Kolb, T. Mair, M. Geller, A. Christmann, R. K. H. Kinne, and K. D. Mathias. In vitro model for the evaluation of inferior vena cava filters: Effect of experimental parameters on thrombus-capturing efficacy of the Vena Tech-LGM filter. *J. Vasc. Interv. Radiol.*, 9:295–304, 1998.

[21] A. A. Katsamouris, A. C. Waltman, M. A. Delichatsios, and C. A. Athanasoulis. Inferior vena cava filters: in vitro comparison of clot trapping and flow dynamics. *Radiology*, 166:361–366, 1988.

[22] E. Komorowicz, K. Kolev, I. Lerant, and R. Machovich. Flow rate modulated dissolution of fibrin with clot-embedded and circulating proteases. *Circ. Res.*, 82:1102–1108, 1998.

[23] R. L. Leask, K. W. Johnston, and M. Ojha. In vitro hemodynamic evaluation of a Simon nitinol vena cava filter: possible explanation of IVC occlusion. *J. Vasc. Interv. Radiol.*, 12:613–8, 2001.

[24] R. L. Leask, K. W. Johnston, and M. Ojha. Hemodynamic effects of clot entrapment in the TrapEase inferior vena cava filter. *J. Vasc. Interv. Radiol.*, 15:485–490, 2004.

[25] P. Lee, A. Raizada, and R. Ciocca. Growing utilization of IVC filter placement from 2001-2005: Analysis of NIS. *Society for Clinical Vascular Surgery*, 2009.

[26] G. D. O. Lowe. Virchow's triad revisited : abnormal flow. *Pathophysiol. Haem. T.*, 33:455–457, 2005.

[27] D. Ma, G. F. Dargush, S. K. Natarajan, E. L. Levy, A. H. Siddiqui, and H. Meng. Computer modeling of deployment and mechanical expansion of neurovascular flow diverter in patient-specific intracranial aneurysms. *J. Biomech.*, 45:2256–63, 2012.

[28] P. E. Marik, M. Baram, and B. Vahid. Does central venous pressure predict fluid responsiveness? *Chest*, 134:172–178, 2008.

[29] S. Nanda, S. P. Bhatt, and M. A. Turki. Inferior vena cava anomalies-a common cause of DVT and PE commonly not diagnosed. *Am. J. Med. Sci.*, 335:409–10, 2008.

[30] OpenCFD Ltd. User Guide, OpenFoam version 2.1.x, 2012.

[31] PREPIC Study Group. Eight-year follow-up of patients with permanent vena cava filters in the prevention of pulmonary embolism: the PREPIC (Prevention du Risque d'Embolie Pulmonaire par Interruption Cave) randomized study. *Circulation*, 112:416–22, 2005.

[32] Z-Y. Qian, M-F. Yang, K-Q. Zuo, J. Cheng, H-B. Xiao, and W-X. Ding. Computed tomography manifestations of common inferior vena cava dysplasia and its clinical significance. *Exp. Ther. Med.*, 5:631–635, 2013.

[33] E. Rahbar, D. Mori, and J. E. Moore. Three-dimensional analysis of flow disturbances caused by clots in inferior vena cava filters. *J. Vasc. Interv. Radiol.*, 22:835–42, 2011.

[34] Z. Ren, S. L. Wang, and M. A. Singer. Modeling hemodynamics in an unoccluded and partially occluded inferior vena cava under rest and exercise conditions. *Med. Biol. Eng. Comput.*, 50:277–87, 2012.

[35] P. J. Roache. *Verification and validation in computational science and engineering.* Hermosa Publishers, Albuquerque, New Mexico, 1998.

[36] R. S. Rosenson, A. McCormick, and E. F. Uretz. Distribution of blood viscosity values and biochemical correlates in healthy adults. *Clin. Chem.*, 42:1189–95, 1996.

[37] D. V. Sakharov and D. C. Rijken. The effect of flow on lysis of plasma clots in a plasma environment. *Thromb. and Haemostasis*, 83:469–74, 2000.

[38] N. C. Sanchez, P. L. Tenofsky, J. M. Dort, L. Y. Shen, S. D. Helmer, and R. S. Smith. What is normal intra-abdominal pressure? *Am. Surgeon*, 67:243–248, 2001.

[39] S. P. Sastry, J. Kim, S. M. Shontz, B. A. Craven, L. C. Frank, K. B. Manning, and T. Panitanarak. Patient-specific model generation and simulation for pre-operative surgical guidance for pulmonary embolism treatment. In *Image-Based Geometric Modeling and Mesh Generation*, pages 227–254. 2013.

[40] M. A. Singer, W. D. Henshaw, and S. L. Wang. Computational modeling of blood flow in the TrapEase inferior vena cava filter. *J. Vasc. Interv. Radiol.*, 20:799–805, 2009.

[41] M. A. Singer and S. L. Wang. Modeling blood flow in a tilted inferior vena cava filter: Does tilt adversely affect hemodynamics? *J. Vasc. Interv. Radiol.*, 22:229–35, 2011.

[42] M. A. Singer, S. L. Wang, and D. P. Diachin. Design optimization of vena cava filters: an application to dual filtration devices. *J. Biomech. Eng.-T. ASME*, 132:101006, 1–10, 2010.

[43] P. B. Sobin. Mechanical properties of human veins. Master's thesis, University of California, 1977.

[44] S. F. C. Stewart, R. A. Robinson, R. A. Nelson, and R. A. Malinauskas. Effects of thrombosed vena cava filters on blood flow: Flow visualization and numerical modeling. *Ann. Biomed. Eng.*, 36:1764–81, 2008.

[45] G. W. Stoneham, B. E. Burbridge, and S. F. Millward. Temporary inferior vena cava filters: In vitro comparison with permanent IVC filters. *J. Vasc. Interv. Radiol.*, 6:731–6, 1995.

[46] T. N. Swaminathan, H. H. Hu, and A. A. Patel. Numerical analysis of the hemodynamics and embolus capture of a greenfield vena cava filter. *J. Biomech. Eng.-T. ASME*, 128:360–70, 2006.

[47] T. K. B. Teo, J. F. Angle, J. I. Shipp, M. K. Bluett, C. A. Gilliland, U. C. Turba, and A. H. Matsumoto. Incidence and management of inferior vena cava filter thrombus detected at time of filter retrieval. *J. Vasc. Interv. Radiol.*, 22:1514–20, 2011.

[48] V. T. Turitto and C. L. Hall. Mechanical factors affecting hemostasis. *Thromb. Res.*, 92:25–31, 1998.

[49] T. W. Wakefield, J. Caprini, and A. J. Comerota. Thromboembolic diseases. *Curr. Probl. Surg.*, 45:844–99, 2008.

[50] S. L. Wang and M. A. Singer. Toward an optimal position for inferior vena cava filters: Computational modeling of the impact of renal vein inflow with Celect and TrapEase filters. *J. Vasc. Interv. Radiol.*, 21:367–74, 2010.

[51] L. Zhang, G. Yang, W. Shen, and J. Qi. Spectrum of the inferior vena cava: MDCT findings. *Abdom. Imaging*, 32:495–503, 2007.

List of Figures

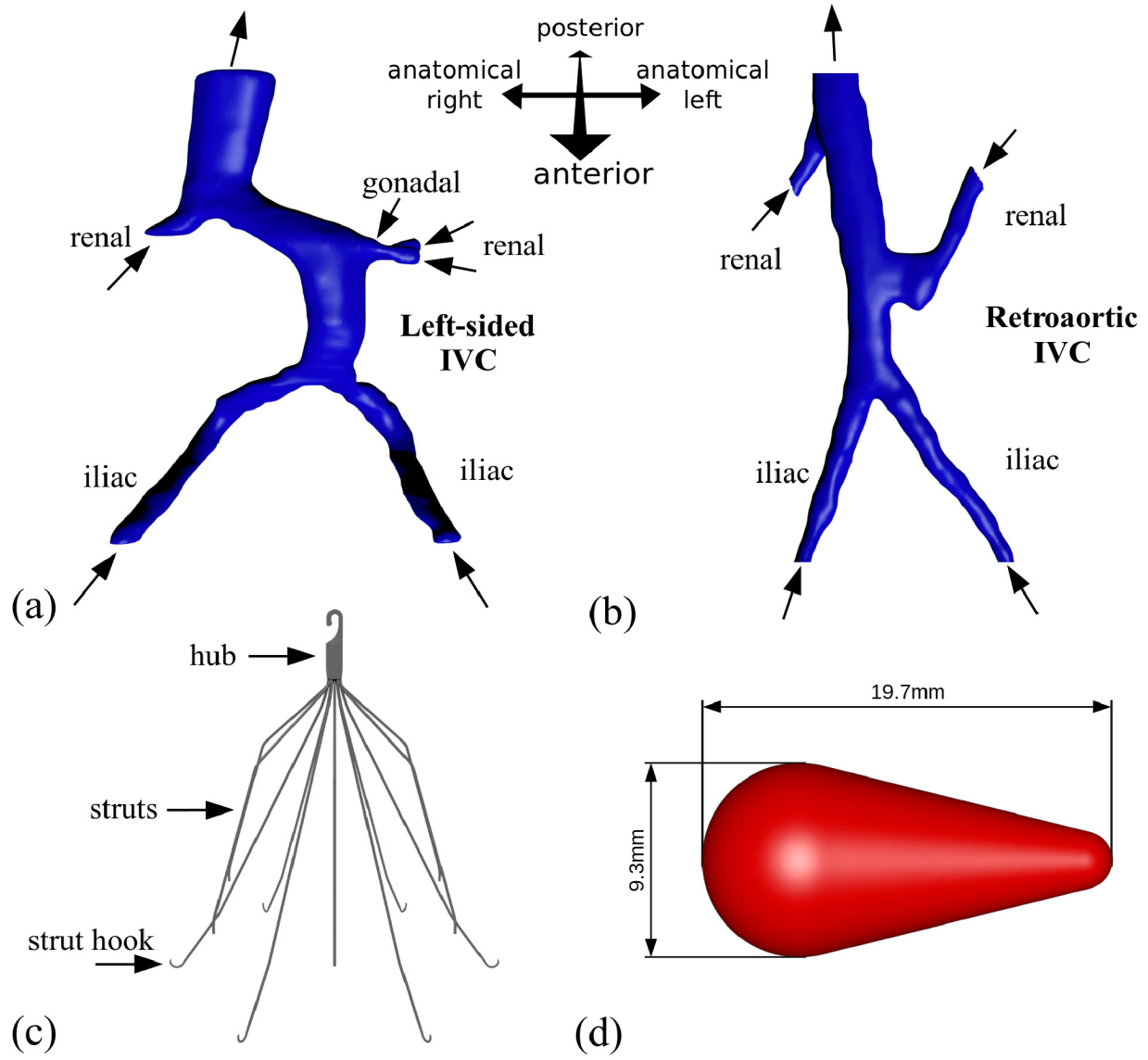

Figure 1 Components used in patient-specific simulations: (a) left-sided IVC, (b) retroaortic IVC, (c) G2 Express IVC filter, and (d) model blood embolus. Posterior and anterior directions are into and out of the page, respectively.

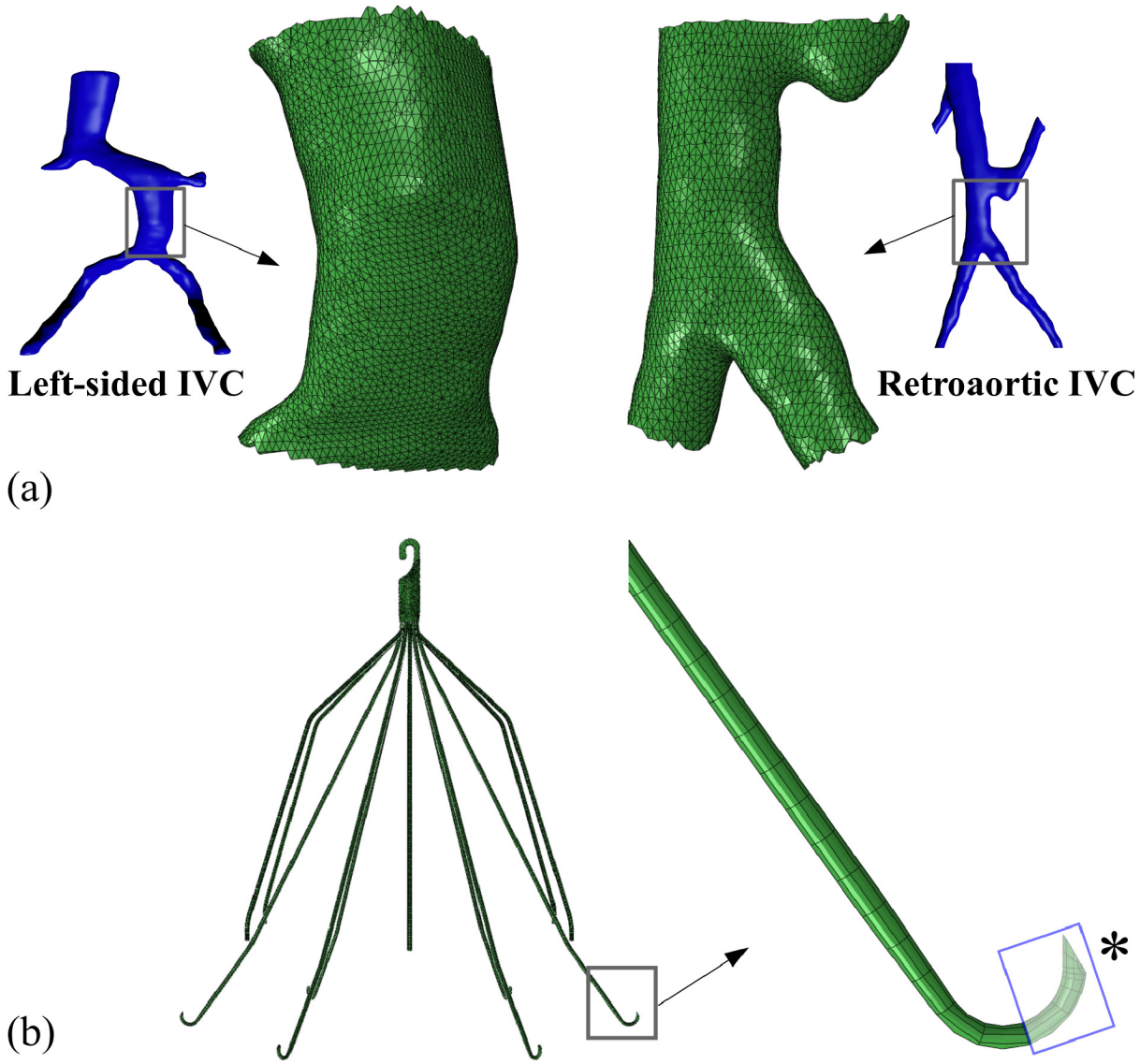

Figure 2 FEA meshes: (a) infrarenal IVC solid meshes derived from the full IVC vein surface meshes; (b) G2 express IVC filter mesh (left), with the hook elements which were not included in the contact simulations highlighted at the asterisk (right).

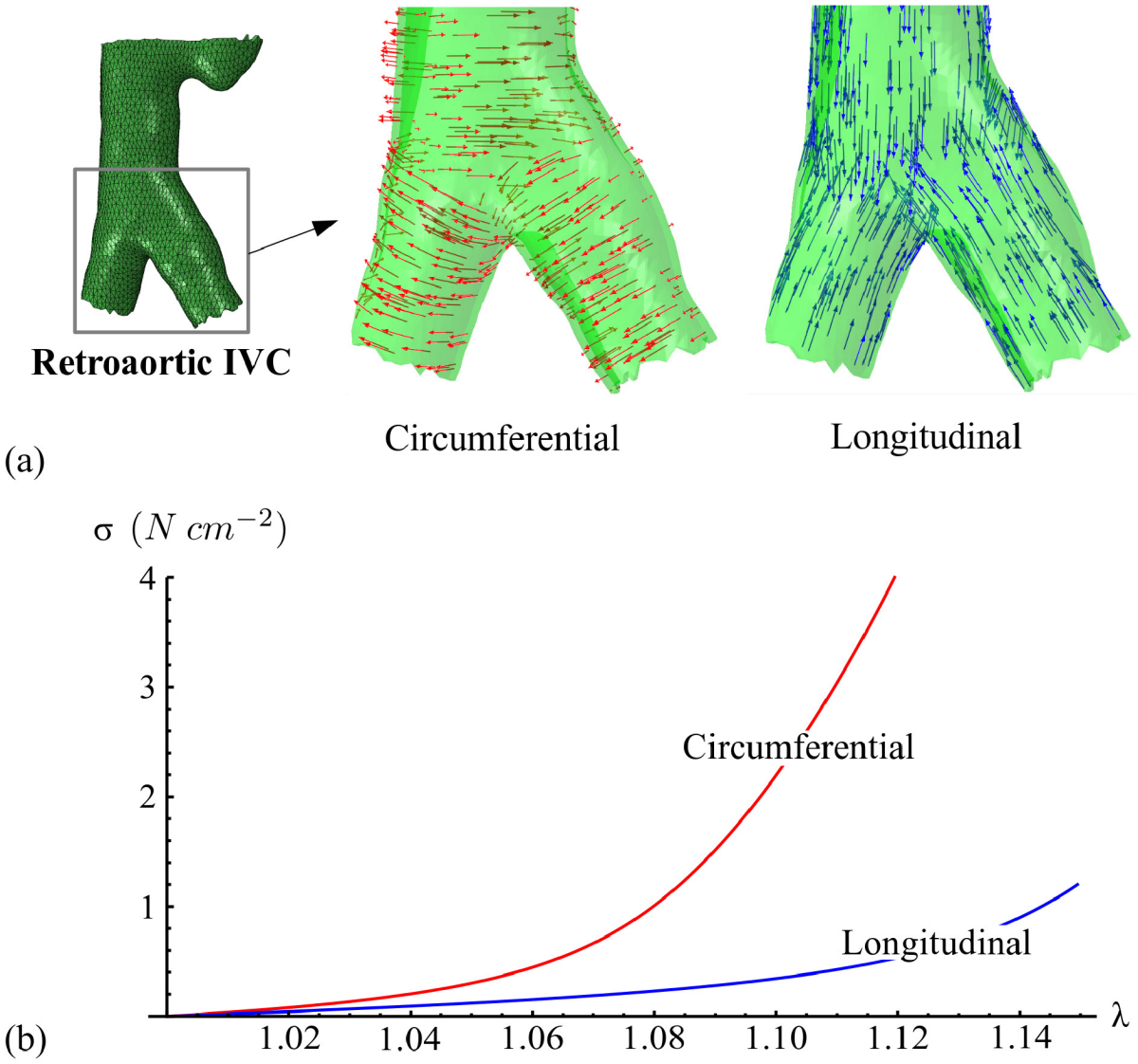

Figure 3 (a) Local material coordinates on the retroaortic IVC mesh; (b) Plot of average stress σ versus stretch λ for human IVC tissue; material properties assigned to veins using the HGO model: $C_{10} = 0.003$, $k_1 = 1.4$, $k_2 = 100$, $\kappa = 0.2$, N = 2, $\gamma = 41.4°$.

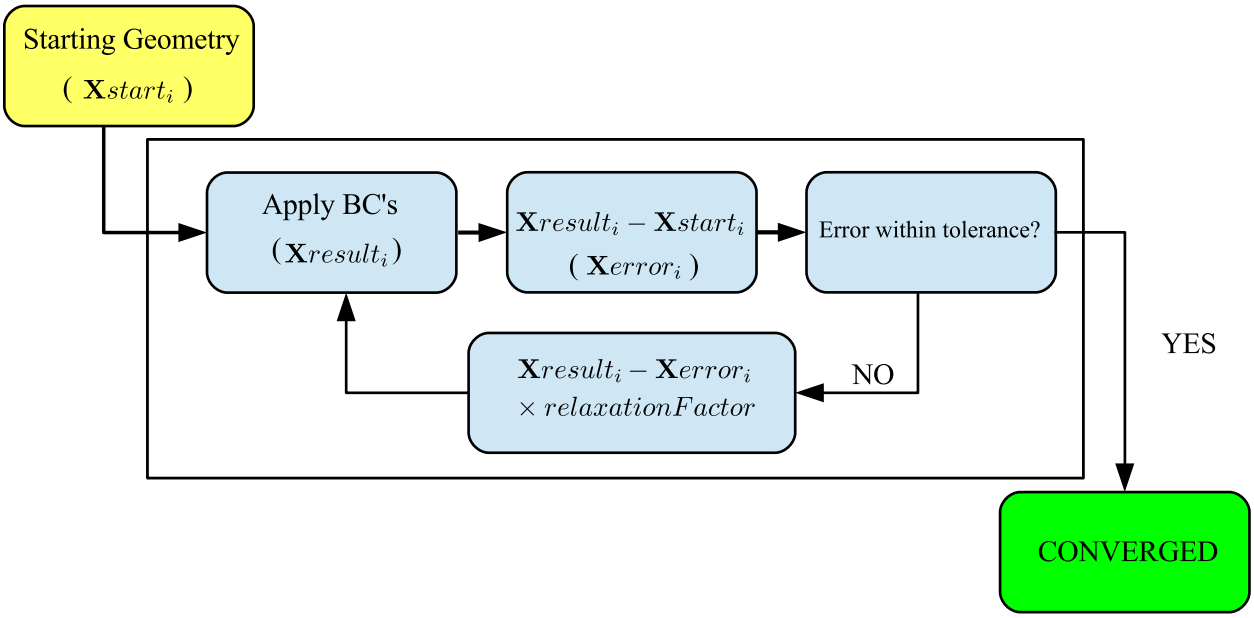

Figure 4 Iterative procedure for performing the inverse analysis to obtain the approximate zero-load state of the patient veins. The variable $\mathbf{X}$ represents the position vector for each node from $i = 1$ to the number of nodes in the vein mesh. Where present, parenthesis indicate the output of a step.

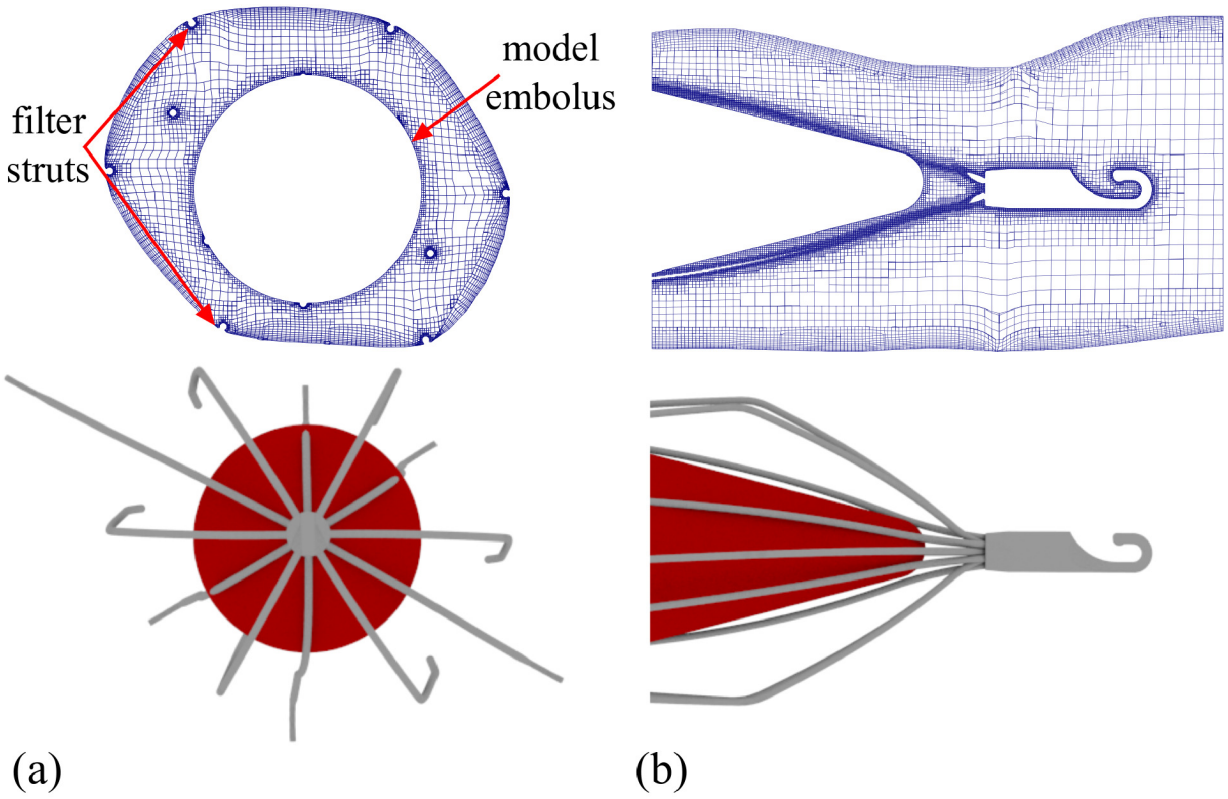

Figure 5 Slices of the fine CFD mesh for the retroaortic case with a placed filter and model embolus: (a) axial plane at max embolus diameter, and (b) mid-plane of placed filter.

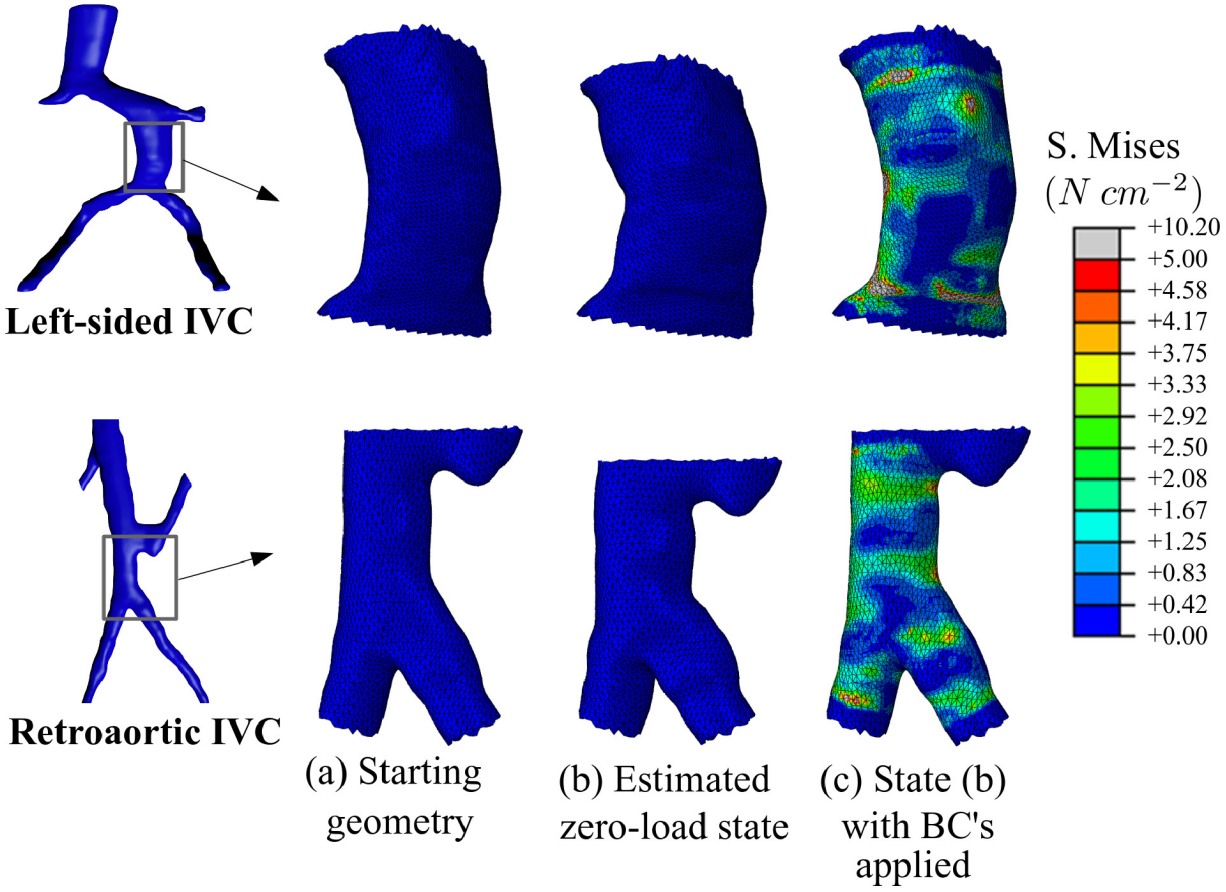

Figure 6 Results from the inverse analyses. Note that the geometry in (c) is nearly identical to that in (a), but (c) provides the approximate *in vivo* stress state.

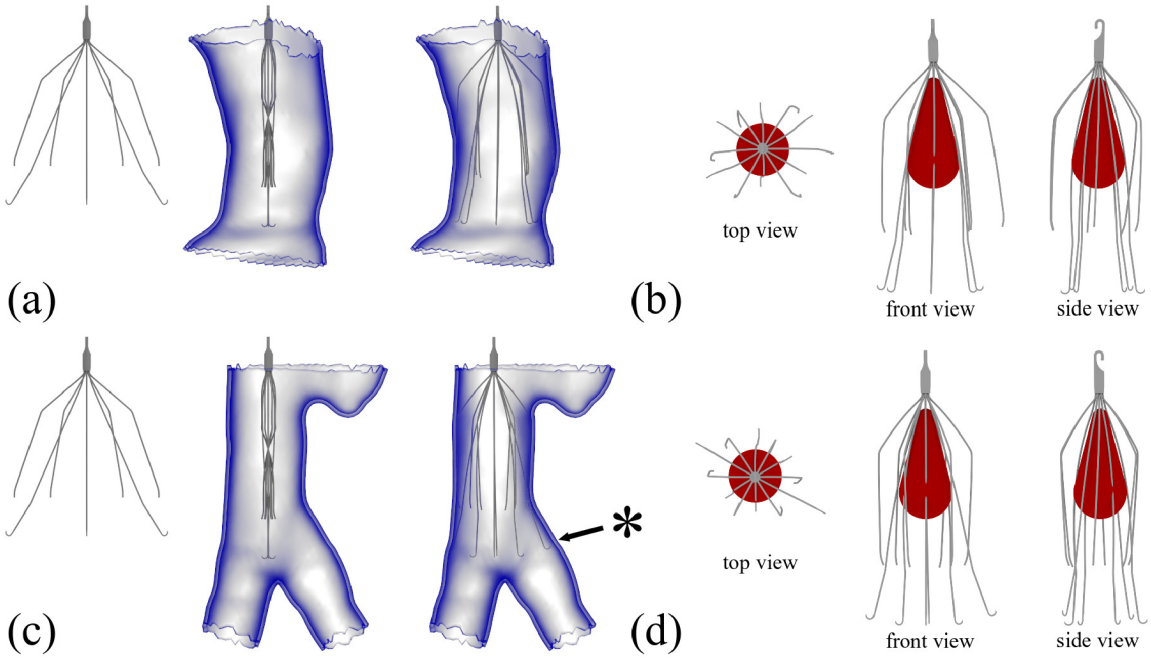

Figure 7 Results of virtual filter and embolus placement in the left-sided (a-b) and retroaortic (c-d) veins. (a,c) Free, sheathed, and placed IVC filter, from left to right. (b,d) Placed IVC filter with model embolus inserted.

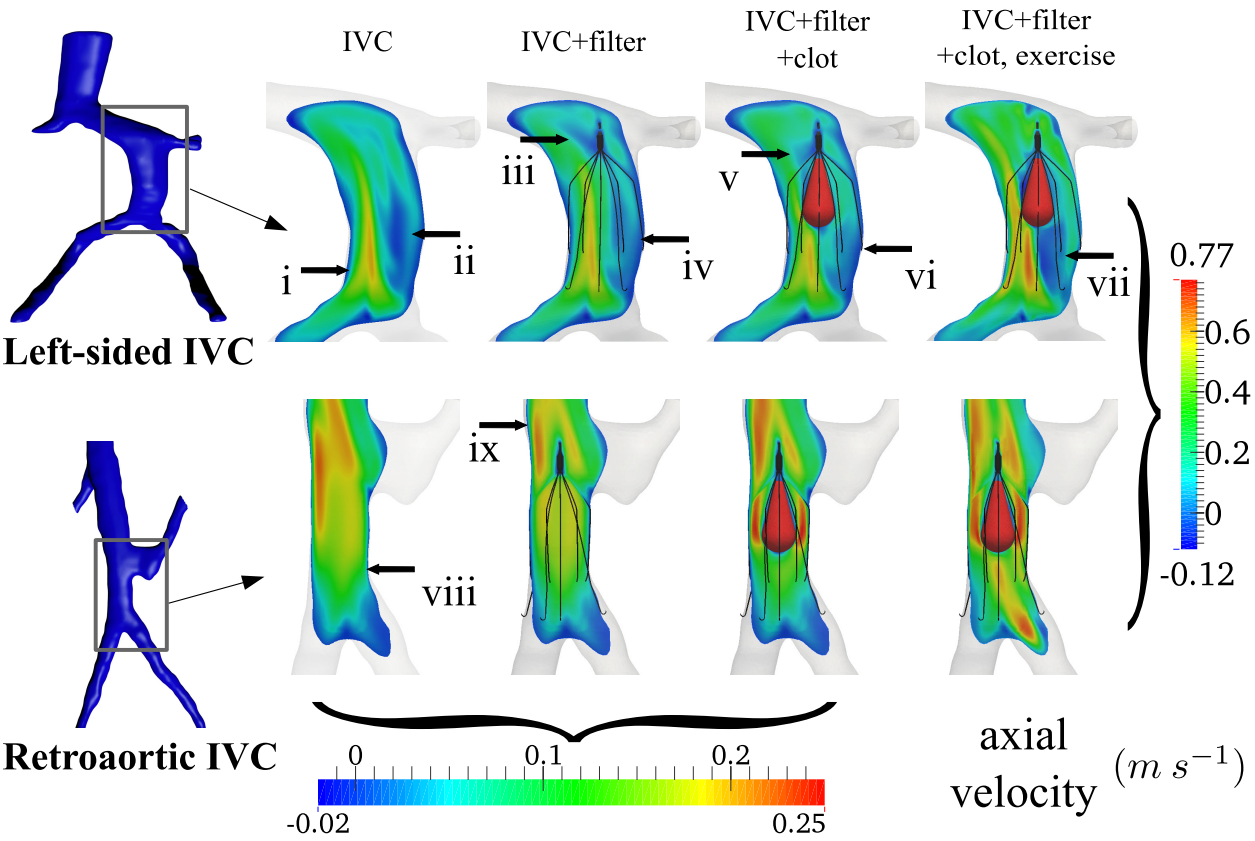

Figure 8 Axial velocity contours on frontal planes at the midpoint of the IVC filter for the left-sided IVC (a) and the retroaortic IVC (b).

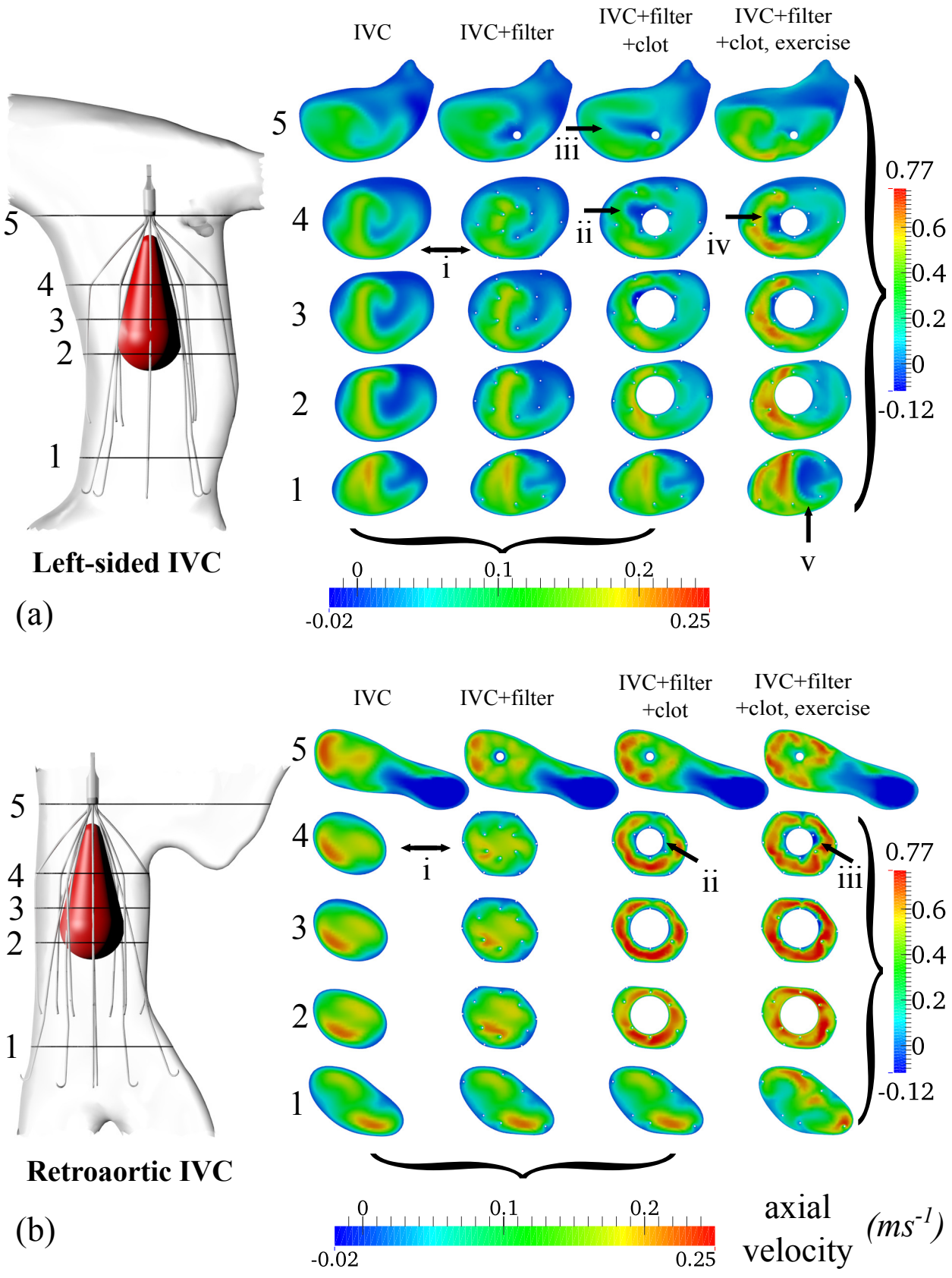

Figure 9 Axial velocity contours on cross sections of the patient veins starting upstream at (1) and proceeding downstream to (5). Slices are oriented with the posterior and anterior directions up and down on the page, respectively.

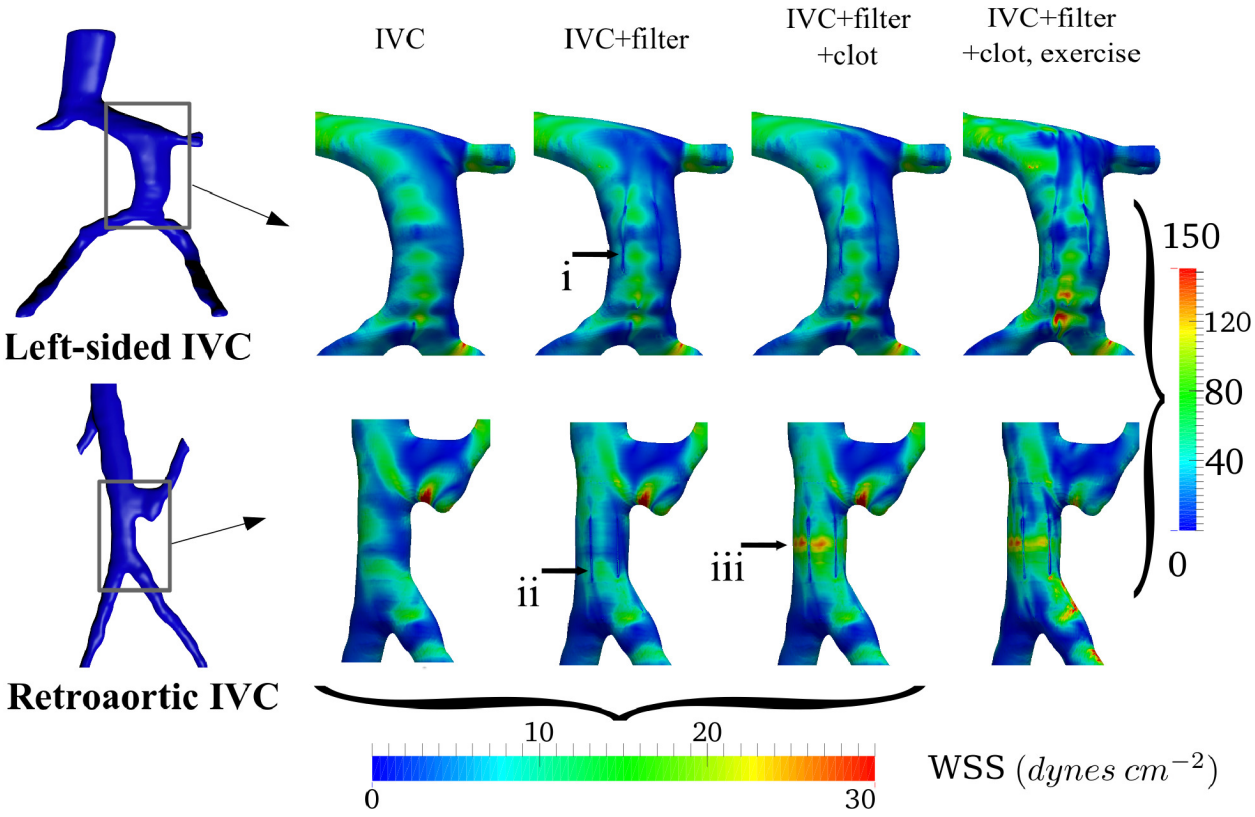

Figure 10 WSS contours on the patient veins near the filter placement site. Low WSS values occur on the IVC near the IVC filter struts; the highest WSS values are observed near the embolus in the retroaortic IVC.

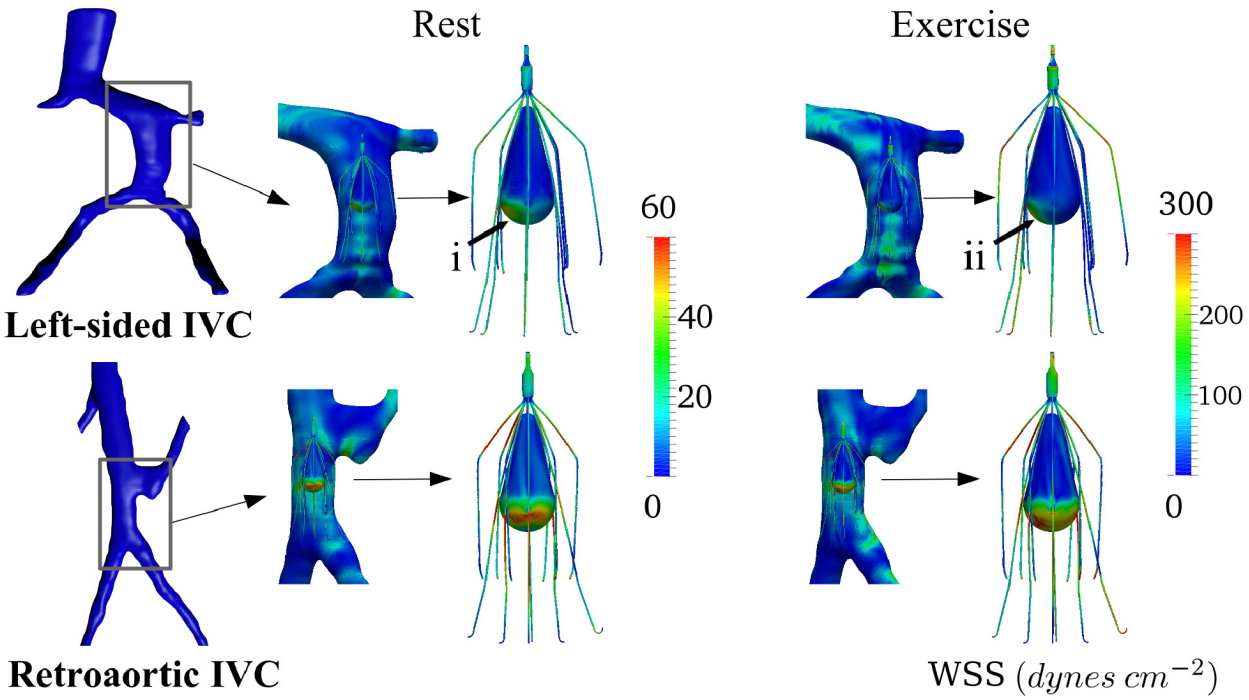

Figure 11 WSS contours on the placed filter and embolus models. High and low WSS values occur on the upstream and downstream portions of the embolus, respectively. In the left-sided IVC, the WSS is highest on the right side of the embolus due to the right-sided jet.

List of Tables

Table 1 Flow rates at rest and exercise flow conditions.[6]

conditions	iliac	infrarenal		renal	suprarenal	
	flow rate	flow rate	Re. No.	flow rate	flow rate	Re. No.
resting	0.6 lpm	1.2 lpm	~300	0.4 lpm	2.0 lpm	~500
exercise	2.0 lpm	4.0 lpm	~1,000	0.75 lpm	5.5 lpm	~1,400